Journal of Materials Chemistry A

ROYAL SOCIETY OF CHEMISTRY

PAPER

View Article Online
View Journal | View Issue

Cite this: J. Mater. Chem. A, 2024, 12, 8516

Electrochemical valorization of HCl for the production of chlorine *via* a proton-filter functional covalent organic framework†

Sukhjot Kaur,‡[a] Kayaramkodath C. Ranjeesh,‡[b] Kalpana Garg,‡[a] Safa Gaber,[b] Shivangi Mehta,[a] Tharamani C. Nagaiah *[a] and Dinesh Shetty *[bc]

Chlorine (Cl_2) is one of the prime building blocks for several industrially important chemicals and engineering materials. HCl electrolysis is a well established technology for the production of Cl_2 at the anode. However, combining it with the hydrogen evolution reaction (HER) at the cathode results in both high energy consumption and safety risks during unexpected shutdowns. Herein, we demonstrated the feasibility of integrating the chlorine evolution reaction (CER) together with the oxygen-depolarized cathode (ODC) by utilizing a nitrogen-rich two-dimensional *in situ* proton filter functional covalent organic framework (COF, **Tta-Dfp**) to suppress the HER. The as-synthesized **Tta-Dfp** COF was explored as a bifunctional catalyst towards the ODC and Cl_2 evolution and exhibited outstanding activity towards Cl_2 evolution with a faradaic efficiency of 92% and demonstrated excellent stability in a corrosive environment even under multiple shut-downs under mimicked industrial conditions. Furthermore, the visualization of the local electrocatalytic activity of the designed COF was analysed by redox competition mode of scanning electrochemical microscopy (RC-SECM) using a Pt ultra-microelectrode and extended to state-of-the-art electrocatalyst, Pt/C (20%). The 3D SECM images demonstrate the excellent stability of the **Tta-Dfp** catalyst in chlorine rich electrolyte. Therefore, metal-free catalysis for Cl_2 production by integrating the two electrochemical processes with the added advantage of energy saving is a promising cost-effective approach.

Received 12th November 2023
Accepted 17th January 2024

DOI: 10.1039/d3ta06948f

rsc.li/materials-a

Introduction

Chlorine (Cl_2) is one of the prime building blocks for several industrially important chemicals and engineering materials which are crucial for day-to-day life. The demand for Cl_2 has increased significantly in the last few decades owing to its excessive use in the fields of polymers, resins, and elastomers and sectors such as healthcare, agro-food, construction, electronics, textiles, transport, and cosmetics.[1–3] The disinfectant capabilities of chlorine have significantly enhanced the quality of life for billions of individuals around the world. Chlorine is a crucial chemical component that is utilized in the production of several products that play a significant role in promoting public health and safety (chlorine-based water and kitchen disinfectants),[4] advancing technology (wind turbine blades, smartphones, hybrid car batteries, *etc.*), enhancing nutrition, ensuring security (bullet-proof vests), and facilitating transportation (shatter-resistant windows, cables, and navigation systems). As reported by the Centers for Disease Control and Prevention (CDC 2020),[5] chlorine is one of the major components that protect swimmers against waterborne pathogens.[6] Also, according to the U.S. Centre for Disease Control and Prevention, the process of adding chlorine to drinking water is considered a highly important advancement in public health in the history of the United States.[7] However, J. J. Rook found that halogenated organic compounds (trihalomethanes, THMs) could be generated as byproducts when chlorine combines with natural organic matter (NOM) in drinking water at a concentration up to ~160 μg L^{-1} of water.[8] Chlorinated surface water was found to be heavily polluted with chlorination by-products in 1975, according to the National Organics Renaissance Survey.[9] Since then, studies have linked drinking chlorinated tap water with high levels of THM to a variety of negative health effects, such as bladder cancer, preterm birth, and miscarriages. But the limit to the level of THM in drinking water has been set to 80 μg L^{-1} by the U.S. under the Stage 1 and 2 Disinfectants and Disinfection Byproducts Rules.[10] At the same time, utilities are combining primary disinfectants such as

[a]Department of Chemistry, Indian Institute of Technology Ropar, Rupnagar, Punjab 140001, India. E-mail: tharamani@iitrpr.ac.in

[b]Department of Chemistry, Khalifa University of Science & Technology, P.O. Box 127788, Abu Dhabi, UAE. E-mail: dinesh.shetty@ku.ac.ae

[c]Center for Catalysis and Separations (CeCaS), Khalifa University of Science & Technology, P.O. Box 127788, Abu Dhabi, UAE

† Electronic supplementary information (ESI) available. See DOI: https://doi.org/10.1039/d3ta06948f

‡ Equal contribution.

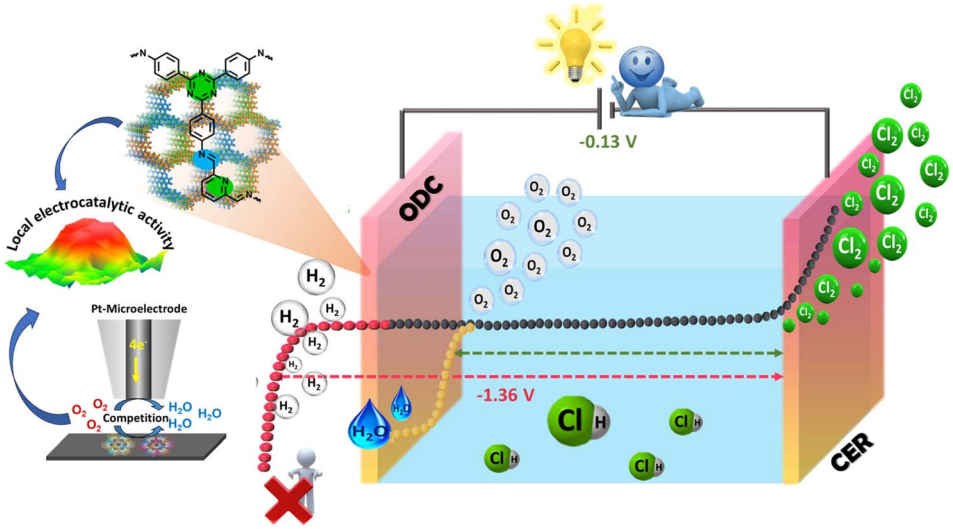

Scheme 1 Schematic representation of the oxygen-depolarized cathode (ODC) coupled chlorine evolution reaction (CER) in HCl electrolysis.

chlorine, ozone, or UV with secondary disinfectants such as chloramines rather than relying only on chlorine disinfection. Such combinations have helped reduce the formation of byproducts in drinking water. There is no doubt that the consumption of disinfection byproducts is fatal; however many alternate ways to utilize chlorine in these applications are being researched and have proven to be beneficial.[11] Being an essential commercial commodity, the demand for Cl_2 production is expected to reach up to approximately USD 27000 by 2030 with a compound annual growth rate (CAGR) of > 3.5% (from 2023 to 2030).[12,13] Various analytical techniques such as the Deacon process[14,15] and chlor-alkali electrolysis have been utilized for the production of Cl_2.[16,17] However, the Deacon process is limited by corrosion, high catalyst demand, limited yields, and low stability,[18,19] while the chlor-alkali process is energy-intensive and consumes 50% of the total production costs.[20] More importantly, chlorine also acts as a strong oxidizing agent in many organic processes and HCl is often released as a byproduct. Globally, 9.3 million tonnes of HCl are produced as byproducts each year, but only 15% is recycled back into Cl_2, leaving an untapped market for Cl_2 recovery that is worth 2.4 billion USD a year.[13] This excess HCl production can be utilized effectively for Cl_2 production rather than just quenching it with lime, which is not eco-friendly and a viable option for the large amount of produced HCl. Therefore, a smart way of valorizing HCl is recycling *via* electrolysis for the production of high-purity Cl_2. HCl electrolysis is composed of the chlorine evolution reaction (CER) at the anode with a potential of 1.36 V *vs.* NHE and hydrogen production at the cathode (HER, $E = 0.00$ V *vs.* NHE) presenting sluggish kinetics with an overall potential of −1.36 V which is energy intensive and raises serious concerns considering the energy crisis.[21,22]

In addition, the critical challenge associated with HCl electrolysis is the accumulation of H_2 and Cl_2 at the cathodic compartment under uncontrolled shutdown as all the membranes show a little permeability to chlorine, creating safety issues.[23–25] These drawbacks can be overcome when the hydrogen production at the cathode is replaced by the oxygen reduction reaction (ORR, $E = 1.23$ V *vs.* NHE) known as the oxygen-depolarized cathode (ODC),[26] while keeping the CER at the anode drastically reduces the cell voltage to −0.13 V compared to the conventional electrolysis ($E_{cell} = -1.36$ V *vs.* NHE), which in turn reduces the significant cost and energy saving by 30% (Scheme 1).[27,28]

Rh_xS_y/C[29] and RuO_2/TiO_2 (ref. 15) have been considered the benchmark catalysts for Cl_2 production, but their cost raises the expense of Cl_2 generation on a pilot scale. On the other hand, Pt/C is the most efficient catalyst currently being studied for the oxygen reduction reaction (ORR);[30,31] however, even in the presence of low chloride ion concentrations, it suffers from catalyst deactivation, poor stability, and dissolution.[32] Till date, not much work has been reported except for a few studies on the ODC which are based on noble metal catalysts *viz.* Pt–Ag[33] and Rh–RhS_x/CNT[23] and non-noble metal catalysts such as vacancy rich $Ni_{2-x}P$,[34] Co-NSC,[35] OCNT-PVIM-ZnPOM,[36], and Cu–Fe_2O_3/NC[37] on the ODC coupled CER. Nevertheless, there is room for improvement in terms of stability and efficient bifunctionality of electrocatalysts for chlorine production.[38,39] The implementation of covalent-organic frameworks (COFs) is revealing novel pathways and effective alternatives in the field of catalysis. These frameworks possess the intriguing ability to precisely adjust their chemical and physical properties at the molecular level through both synthetic and post-synthetic modifications.[40–45] Adding to their positives, these framework materials show remarkable stability in corrosive acidic media. Recently, they have been utilised as efficient catalysts for the oxidative desulfurisation process.[46] Moreover, with the focus on replacing the HER with the ODC, the emerging tunable proton-filter properties of COFs have been utilized to suppress the production of hydrogen (H_2) and increase oxygen (O_2) or nitrogen (N_2) concentrations near the electrode surface.[45,47] Hence, the implementation of a unified system incorporating *in situ* proton filtration and a catalytic centre has the potential to streamline electrode structures and enhance overall efficiency.

Herein, we have explored nitrogen-rich two-dimensional *in situ* proton filtering **Tta-Dfp** COF as a bifunctional electrocatalyst for HCl oxidation and the oxygen reduction reaction. However, to the best of our knowledge this **Tta-Dfp** is the first metal free based catalyst for HCl electrolysis, which can perform both oxygen reduction (as ODC) and Cl_2 evolution. Typically, in the pursuit of electrocatalyst advancement, conventional electrochemical methodologies such as cyclic voltammetry and rotating disc electrode measurements are commonly utilised to assess the efficacy of catalyst performance. Recently, the utilisation of scanning electrochemical microscopy (SECM) has extended to the assessment of localised catalytic activity.[33,35] Presently, the in-depth analysis of the activity of the catalyst for the ORR in chorine rich media in comparison to state-of-the-art Pt/C was studied using SECM along with stability under mimicked industrial conditions.

Experimental details

Synthesis of Tab-Dfp. Tab-Dfp was synthesized by using a reported method with slight modifications.[45,48,49] The synthesis procedure consisted of the Schiff base condensation reaction of 2,6-diformylpyridine (Dfp) (11.53 mg, 0.085 mmol) and 1,3,5-tris(4-aminophenyl) benzene (Tab) (20 mg, 0.056 mmol) in 2 mL of a 1,4-dioxane/mesitylene mixture (1 : 1 v/v ratio). The reaction was conducted in a sealed pressure tube with a catalytic amount of acetic acid (50 μl, 6 M aqueous). After heating at 120 °C for five days, the yellow precipitate was collected by centrifuging and washed several times with *N*,*N*-dimethylacetamide (DMA), water, and acetone to remove any impurities and unreacted products. This was followed by drying the sample at 80 °C for 12 hours under vacuum. **Tab-Dfp** COF was obtained as a yellow solid with 79% of the isolated yield (Fig. S1a†).

Synthesis of Tta-Dfp. Tta-Dfp was synthesized by following the reported literature with minor modifications.[41,43,45,50] The synthesis involved the Schiff base condensation of 4,4′,4″-(1,3,5-triazine-2,4,6-triyl)trianiline (Tta) (20 mg, 0.056 mmol) and 2,6-diformylpyridine (Dfp) (11.43 mg, 0.084 mmol) in 2 mL of a 1,4-dioxane/mesitylene mixture (1 : 1 v/v ratio). The reaction was conducted in a sealed pressure tube with a catalytic amount of acetic acid (50 μl, 6 M aqueous). After heating at 120 °C for five days, the yellow precipitate was collected by centrifuging and washed several times with *N*,*N*-dimethylacetamide (DMA), water, and acetone to remove any impurities and unreacted products. This was followed by drying the sample at 80 °C for 12 hours under vacuum. **Tta-Dfp** COF was obtained as a yellow solid with 82% isolated yield (Fig. S1b†).

Electrochemical investigation. The electrochemical measurements were performed using a three-electrode assembly consisting of as-synthesized catalyst-coated carbon paper (0.5 × 0.5 cm), a graphite rod, and Ag/AgCl/3 M KCl as the working, counter, and reference electrode respectively. The cyclic voltammetry (CV) and linear sweep voltammetry (LSV) experiments were performed using a Biologic (VSP 300) potentiostat/galvanostat with a FRA7M module, controlled with EC-Lab V11.12 software. Linear sweep voltammetry (LSV) was performed in 0.4 M HCl (pH = 1) with a scan rate of 5 mV s^{-1} across a potential range of 1.0 to 2.0 V *vs.* RHE with constant stirring of 500 rotations per minute (rpm). Additionally, the chronoamperometric stability test was performed @ 1.5 V for 24 h.

Results and discussion

Material characterisation

The microstructural attributes of **Tta-Dfp** and **Tab-Dfp** were analyzed using powder X-ray diffraction (PXRD) patterns (Fig. 1a), wherein they displayed two distinct peaks: the peak at $2\theta = 5.0°$ can be attributed to the (110) plane of the regularly ordered lattice and the broad peak centered at $2\theta = 25.7°$ is attributed to the reflection from the (003) plane. Moreover, the best agreements between the experimental and simulated PXRD patterns were found for the layer-stacked structures (Fig. 1b) with an ABC sequence (Fig. S2,† R_{wp} = 3.19% and R_p = 4.85%, Table S1†).[41,43,45,50] Fourier-transform infrared (FT-IR) spectra confirm the formation of imine (C═N) bonds by revealing a stretching vibration at 1690 cm^{-1} for both **Tta-Dfp** and **Tab-Dfp** (Fig. 1c). On comparison of FT-IR spectra of pristine monomers, the stretching bands corresponding to the aldehyde (1720–1735 cm^{-1}) and the amine group (3300–3400 cm^{-1}) were significantly attenuated in both COFs indicating successful imine condensation (Fig. S3†).[41,43,50] It is important to note that COF polymerization may not be completely terminated and therefore a trace amount of peak was observed at 1720–1735 cm^{-1} for both **Tta-Dfp** and **Tab-Dfp**, which might have resulted from unreacted peripheral end functional groups in the 2D growth of COFs along with the possible defect sites.[41,43,45,50] Afterward, ^{13}carbon cross-polarization magic-angle spinning nuclear magnetic resonance (CP-MAS NMR) spectroscopy (Fig. S4 and S5†) presented a distinctive peak at ∼157 ppm corresponding to imine carbon (–C═N), confirming the **Tab-Dfp** and **Tta-Dfp** formation.[41,43,45,48–50] The carbon atoms of the phenyl, triazine, and pyridine groups are responsible for the signals at 120, 126, 130, 150, and 167 ppm respectively, confirming the **Tta-Dfp**'s chemical structure. Similarly, the carbon atoms of the pyridine and phenyl rings of the **Tab-Dfp** structure are responsible for the signals at 147, 136, 126, 121, 114 ppm, confirming the **Tab-Dfp**'s chemical structure. The UV-vis spectra of **Tta-Dfp** showed peaks at 430 and 475 nm which could be attributed to the π–π* transition of pyridine and n–π* transition of triazine, respectively, along with a broad band at 525 nm resulting from the delocalized π-electron cloud of **Tta-Dfp** (Fig. S6†). **Tta-Dfp** demonstrates its thermal stability up to 400 °C with < 10% weight loss (Fig. S7†) witnessed by thermogravimetric analysis (TGA). Furthermore, the N_2 adsorption studies of **Tta-Dfp** and **Tab-Dfp** showed type-II adsorption isotherms with a Brunauer–Emmett–Teller (BET) surface area of 417.2 m^2 g^{-1} (Fig. S8†) and 368.4 m^2 g^{-1} (Fig. S10†) respectively.[45–47,50] Besides, **Tta-Dfp** and **Tab-Dfp** exhibited a maximum pore size distribution of 1.53 nm and 1.55 nm respectively which are consistent with the suggested structural model and reported literature (Fig. S9 and S11†).[45,48,49]

The morphological aspects of **Tta-Dfp** and **Tab-Dfp** by field emission-scanning electron microscopy (FE-SEM) revealed spherical morphology with spikes (Fig. S12†). While high-resolution transmission electron microscopy (HR-TEM, Fig. 1d)

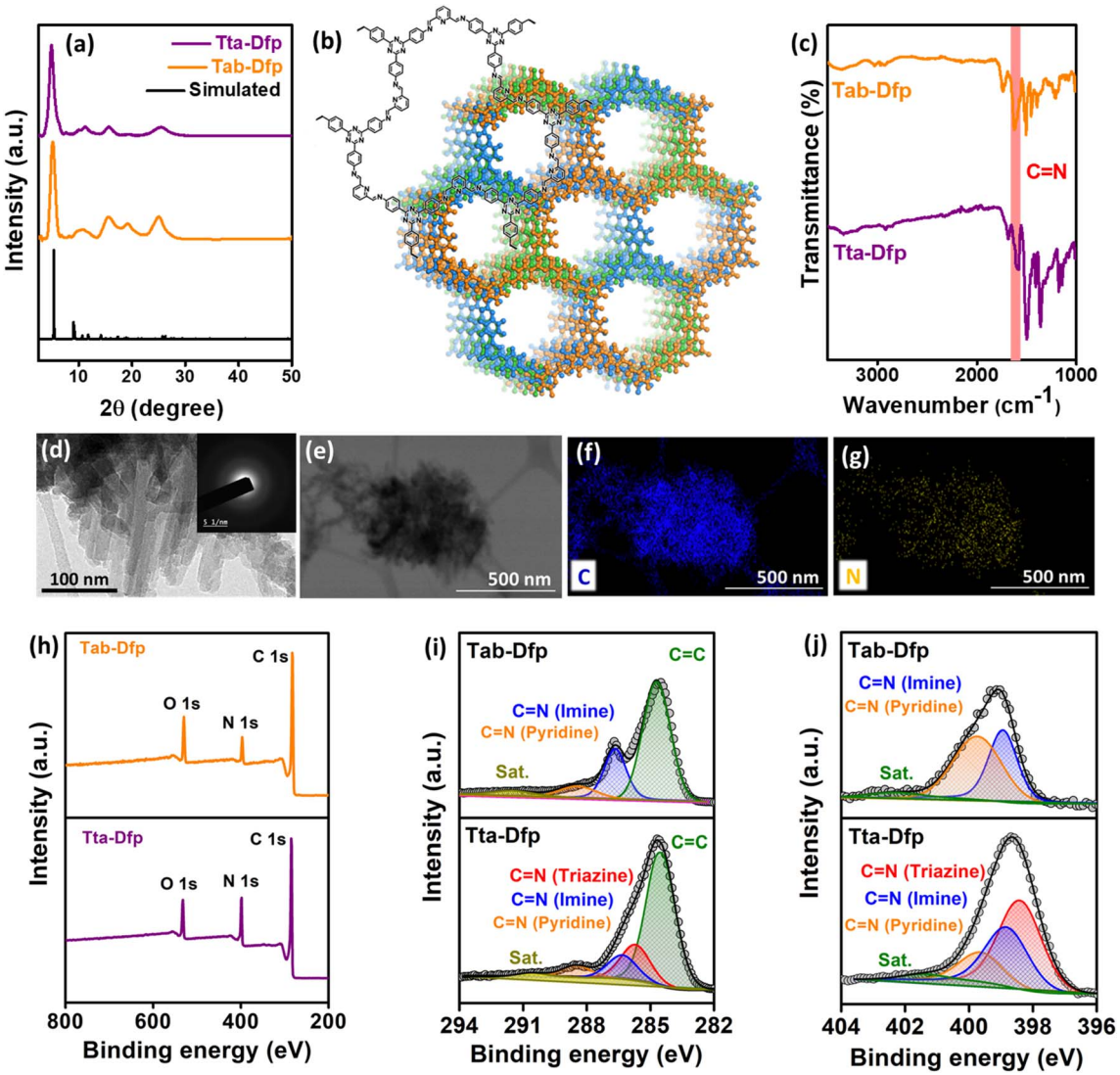

Fig. 1 (a) Experimental and simulated P-XRD patterns of **Tta-Dfp** and **Tab-Dfp**,[45] (b) ChemDraw and simulated structures of **Tta-Dfp**, (c) FT-IR spectra of **Tta-Dfp** and **Tab-Dfp** representing the formation of imine linkages, (d) HR-TEM image of **Tta-Dfp** (inset displaying the SAED pattern), (e–g) TEM-EDS scanned area and dot mapping images showing C and N, (h) XPS survey spectra, and deconvoluted (i) C 1s and (j) N 1s of **Tta-Dfp** and **Tab-Dfp**.[45]

exhibited a layered sheet-like/rod structure and the existence of diffuse rings in the selected area electron diffraction (SAED, inset, Fig. 1d) pattern confirms the amorphous nature of **Tta-Dfp**. As expected, the EDS (energy dispersive X-ray spectroscopy) dot mapping by both SEM and TEM confirms the presence of carbon and nitrogen which are dispersed homogeneously (Fig. 1e–g and S13†).[45] Table S2† shows the weight percentage of C and N using EDS spectral analysis and CHN–O analysis which revealed the higher percentage of N content in **Tta-Dfp** due to the presence of triazine groups. The X-ray photoelectron spectroscopy (XPS) survey spectra of both **Tta-Dfp** and **Tab-Dfp** catalysts showed peaks at a binding energy (BE) of ~284 eV, 396.9 eV and 532 eV attributing to the presence of C 1s, N 1s, and O 1s respectively (Fig. 1h). The difference in the intensity of the N 1s peak at 396.9 eV provided confirmation for the presence of a higher atomic ratio of N in **Tta-Dfp** as compared to **Tab-Dfp**.[45] The deconvoluted C 1s XPS spectra in both **Tta-Dfp** and **Tab-Dfp** showed the presence of aromatic C=C, C=N (imine linkage), C=N (pyridine) and a carbon satellite at a BE value of 284.5, 286.4, 288.1 and 290.3 eV respectively (Fig. 1i). However, **Tta-Dfp** specified the presence of C=N (triazine) at a BE value of 285.7 eV, which was not perceived in **Tab-Dfp**. Moreover, N 1s XPS spectra in **Tta-Dfp** upon deconvoluting exhibit three peaks at a BE of 398.4, 398.8, 399.6 and 401.2 eV corresponding to C=N (triazine), C=N (imine), C=N (pyridine) and a satellite peak respectively (Fig. 1j), whereas **Tab-Dfp** signified the absence of the triazine moiety in its structure.

Electrochemical analysis

Chlorine evolution reaction. To understand the efficacy of the synthesized **Tta-Dfp** and **Tab-Dfp** catalysts towards chlorine production, primarily linear sweep voltammetry (LSV)

experiments were performed in 0.4 M HCl in the potential range of 1.0 V to 2 V *vs.* RHE at a scan rate of 25 mV s^{-1} under continuous stirring in order to remove bubble formation at the electrode surface. As can be seen in Fig. 2a, a sharp increase in the current density for **Tta-Dfp** at *ca.* 1.5 V *vs.* RHE was observed with a current density of 160 mA cm^{-2} at 2.0 V *vs.* RHE which can be ascribed to the oxidation of chloride (Cl^-) ions to chlorine (Cl_2) further evident by the bubbles on the electrode due to evolution of chlorine gas, whereas **Tab-Dfp** exhibited relatively lower activity w.r.t. Cl^- oxidation witnessed by a lower current density (cd) of 91 mA cm^{-2} @ 2.0 V *vs.* RHE. To validate whether the oxidation process is due to the Cl_2 evolution reaction (CER), an additional experiment was performed in a chlorine-free environment, *i.e.*, 0.2 M H_2SO_4. As depicted in Fig. 2b the oxidation process started at a potential of *ca.* 1.73 V *vs.* RHE and reached only 28 mA cm^{-2} of cd @ 2.0 V. This clearly demonstrated that the oxidation process in HCl media is due to the CER while in H_2SO_4, it is due to the oxygen evolution reaction (OER). This further signified the fact that the catalyst is selective towards the CER and there is no interference from the OER during the chlorine production. Additionally, LSVs were recorded for the benchmark CER electrocatalysts (RuO_2 and Rh_xS_y/C) under the same experimental conditions. It was observed (Fig. S14A†) that RuO_2 exhibited the highest electrocatalytic activity and interestingly, **Tta-Dfp** demonstrated activity comparable to that of the benchmark catalysts.

Furthermore, to investigate the faster kinetics of the electrode towards the potential-dependent electrocatalytic reaction, the Tafel slope was evaluated (Fig. S14B†). The lower Tafel slope of 348 mV dec^{-1} for **Tta-Dfp** compared to that for **Tab-Dfp** (402 mV dec^{-1}) depicted the enhanced adsorption/desorption of intermediate species. The superior electrocatalytic activity of **Tta-Dfp** over **Tab-Dfp** may be attributed to the facile charge transfer at the electrode–electrolyte interface, which was estimated by electrochemical impedance spectroscopy (EIS). EIS spectra (Fig. S15 and Table S3†) show a lower charge transfer resistance (R_{ct}) of 190.2 Ω (obtained from fitting the Nyquist plots using an equivalent circuit as shown in Fig. S16†) and a higher rate constant (1.40×10^{-5} cm s^{-1}) for **Tta-Dfp** signified faster charge transfer kinetics accelerating the electrochemical activity.

This could be attributed to the higher surface area of **Tta-Dfp** (Fig. S9†) and the exposure of more electrocatalytic active sites which was supported by the electrochemical surface area (ESCA, mm^2) and specific surface area (SSA, mm^2 mg^{-1}) analyses. The higher ESCA (2.70 mm^2) and SSA (22.5 mm^2 mg^{-1}) of **Tta-Dfp** in comparison to **Tab-Dfp** (Fig. S17 and Table S4†) validated the above conclusion. This was supported by chronoamperometry sequential (Fig. 2c) analysis performed at different potentials for 10 min each in 0.2 M H_2SO_4 and 0.4 M HCl. An increase in current density at 1.5 V in Cl^- rich environments compared to that under Cl^- free conditions confirmed the incompetence of the OER with the CER.

Assessment of evolved chlorine. Furthermore, sequential chronoamperometric experiments were performed using a bipotentiostatic four-electrode assembly as shown in Fig. 2d. Experiments were carried out using catalyst-coated carbon paper as working electrode 1 (WE1, substrate), a Pt microelectrode (Ø 25 μm) as WE2, aligned perpendicular to WE1, while Ag/AgCl/3 M KCl served as the RE, and a graphite electrode as the CE. The measurements were carried out by polarizing WE1 from 1.0 to 1.6 V *vs.* RHE in the region of chlorine oxidation with an interval of 100 mV for 10 min each to invoke Cl_2 oxidation, whereas WE2 was constantly polarised at 0.9 V *vs.* RHE (which

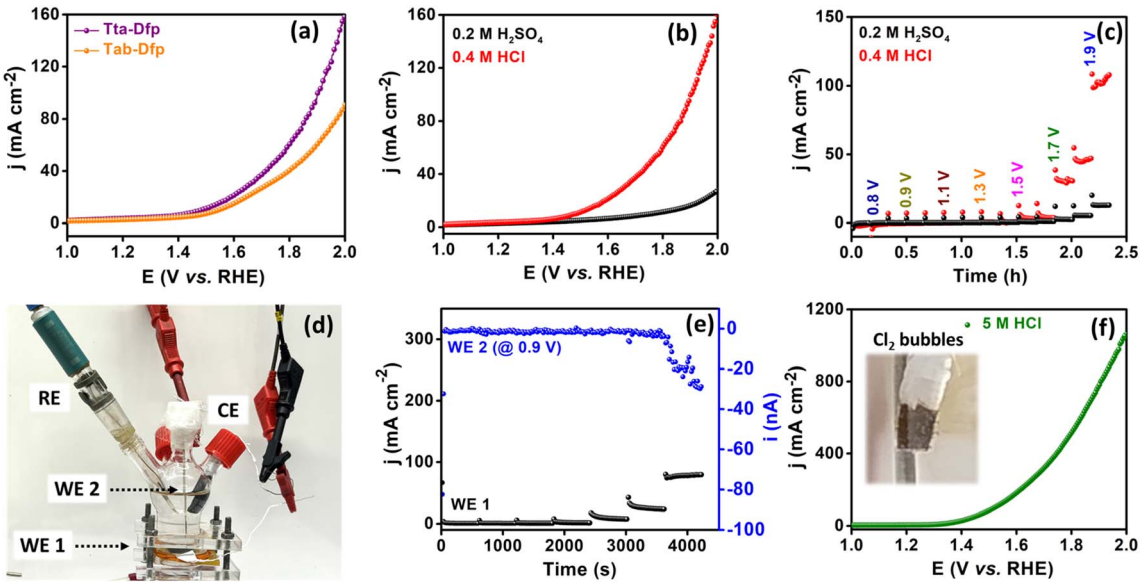

Fig. 2 (a) LSV curves of **Tta-Dfp** and **Tab-Dfp** in 0.4 M HCl electrolyte, (b) LSV curves of **Tta-Dfp** in 0.4 M HCl and 0.2 M H_2SO_4 electrolyte, (c) sequential chronoamperometry for Cl_2 and O_2 evolution in 0.4 M HCl and 0.2 M H_2SO_4 electrolyte respectively, (d) photographic image depicting the homemade cell set up consisting of WE1, WE2, RE and CE in 0.4 M HCl electrolyte for four electrode studies, (e) sequential chronoamperometry for Cl_2 evolution at the WE1 (**Tta-Dfp** catalyst coated substrate) and chlorine reduction reaction (CRR) at WE2 (Pt tip) in 0.4 M HCl electrolyte, and (f) LSV curve for **Tta-Dfp** in 5 M HCl electrolyte (inset displaying Cl_2 bubbles).

corresponded to the chlorine reduction to Cl^-) to detect the *in situ* generated Cl_2. As observed from Fig. 2e, initially the absence of chlorine was witnessed from constant cd at both WE1 and WE2 when the potential was swept from 1.0 to 1.4 V. As WE1 polarized towards more positive *i.e.*, at 1.5 V *vs.* RHE, a steep increase in the cd was observed at WE1 and simultaneously, the reduction current at the tip (WE2) started to increase, which marked the onset of the Cl_2 production at the sample, *i.e.*, WE1.

The produced Cl_2 was further quantified using the iodometric titration method (calculations detailed in the ESI), exhibiting a high amount of Cl_2 produced with a F.E. of 92%. Furthermore, the long-term stability was studied for 200 LSV cycles wherein a negligible change in the potential and cd which is further complemented by the chronoamperometry curve @ 1.5 V *vs.* RHE for 50 h (Fig. S18†) imposed high catalyst durability in corrosive HCl environments. Afterward, to understand the stability of the proposed catalyst under highly acidic conditions, the activity of **Tta-Dfp** towards the CER was probed by measuring the LSV curve in 5 M HCl (Fig. 2f), and strikingly, a high current density of about 1058 mA cm^{-2} was obtained at 2 V *vs.* RHE and the produced chlorine (Cl_2) was evident by bubbles on the electrode (inset Fig. 2f).

Oxygen depolarised cathode. As discussed above, the ODC-coupled CER would prove to be energy efficient for HCl electrolysis; therefore, the electrocatalytic ability of **Tta-Dfp** and **Tab-Dfp** was also evaluated for the oxygen reduction reaction (ORR). Electrochemical measurements were performed to investigate the ORR performance of **Tta-Dfp** and **Tab-Dfp** in 0.4 M HCl solution using a standard three-electrode electrochemical cell. Initially, linear sweep voltammetry (LSV) was performed under hydrodynamic conditions in Ar and O_2 saturated 0.4 M HCl electrolyte in the potential range of 0.5 V to −0.1 V *vs.* RHE at a scan rate of 10 mV s^{-1}. The LSV curves of **Tta-Dfp** in Fig. 3a showed an increase in the reduction cd around 0.3 V *vs.* RHE when the electrolytic solution was saturated with oxygen, which was completely absent when oxygen was degassed upon purging with argon, implying the activity of the catalyst towards the ORR. Moreover, **Tta-Dfp** displayed superior performance in contrast to **Tab-Dfp** as shown in Fig. 3b. This could be due to the higher surface area, high nitrogen atomic percentage and large pore volume of the triazine-based covalent framework of **Tta-Dfp**[51–54] as discussed above.

Furthermore, rotating disc electrode (RDE) tests were conducted to ascertain the kinetic characteristics of both variants towards the ORR. The RDE measurements were carried out by sweeping potential cathodically from 0.4 V to −0.1 V *vs.* RHE in O_2 saturated 0.4 M HCl at a scan rate of 10 mV s^{-1} at different rotation rates varying from 0 to 1300 rpm (rotations per minute, Fig. S19A(a and b)†). The kinetic parameters were evaluated, using the Koutecky–Levich (K–L) equation. As can be seen from

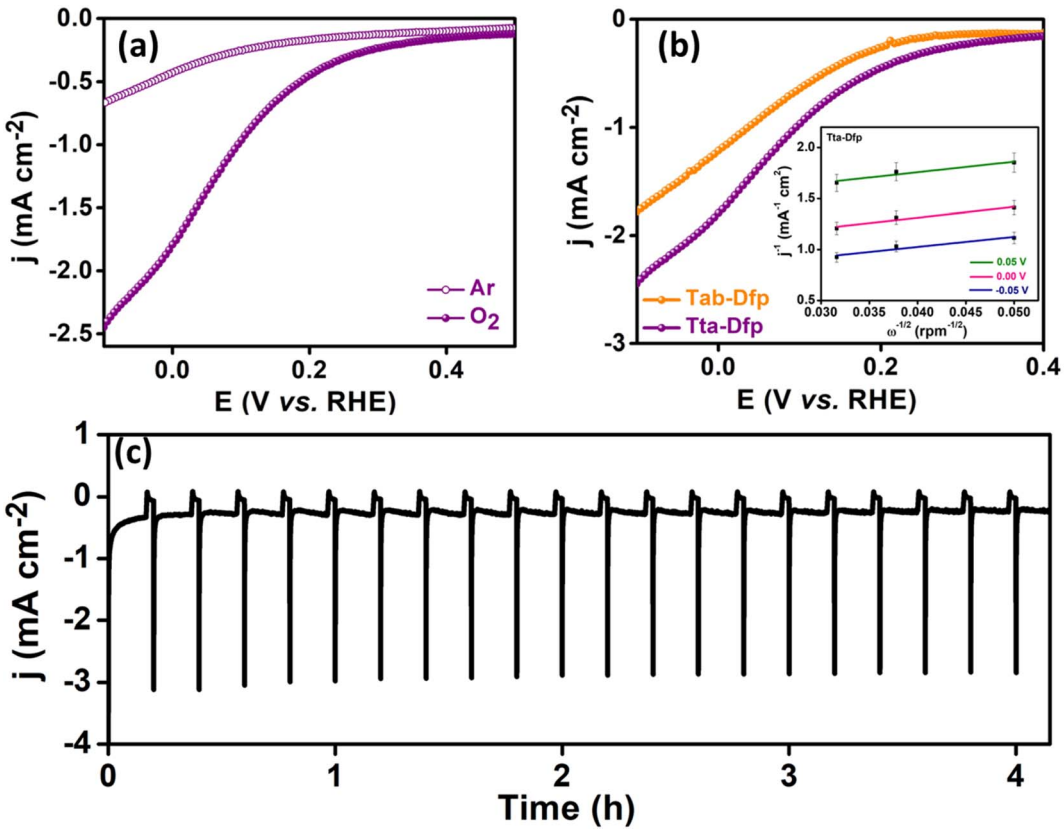

Fig. 3 (a) LSV curves for **Tta-Dfp** in Ar and O_2 saturated 0.4 M HCl electrolyte for the ORR at a rotation rate of 400 rpm, (b) LSV curves of **Tta-Dfp** and **Tab-Dfp** in O_2 saturated 0.4 M HCl electrolyte (inset displaying the K–L plot for **Tta-Dfp**) at a rotation rate of 400 rpm, and (c) chronoamperometric analysis performed for 10 minutes of operation at 0.0 V and 2 minutes of shutdown (*i.e.* system off) for the **Tta-Dfp** catalyst.

the K–L plots in Fig. S19c and d,† a linear relation was observed between the inverse of current density (j^{-1}) and square root of the inverse of the rotation rate ($\omega^{-1/2}$) at various potentials (0.05 V, 0.00 V and −0.05 V *vs.* RHE), indicating the first order kinetics of the reaction. The number of electrons transferred was found to be 3.5 at 0.05 V *vs.* RHE for **Tta-Dfp**. Besides its high activity, stability studies were also carried out under the mimicked industrial shutdown conditions. For the same, chronoamperometric measurements were performed for 10 minutes of operation towards the ORR at 0.0 V *vs.* RHE followed by 2 minutes of shutdown at open circuit potential (OCP) in the Cl_2 and O_2 rich environment. As can be seen from Fig. 3c, the current response obtained for **Tta-Dfp** remains stable even after 20 shutdown cycles (4 hours) exhibiting high retention in the activity. Similarly, 10 shutdown cycles were recorded for benchmark electrocatalysts but as shown in Fig. S19B,† the current density relatively decreased in the first few cycles pointing towards their comparatively lower stability in corrosive HCl environments.

Scanning electrochemical microscopic (SECM) analysis. Furthermore, to gain in-depth insights into the catalyst surface with high spatial resolution in terms of active site distribution the stability of **Tta-Dfp** and **Tab-Dfp** towards the ORR in chlorine rich electrolyte was evaluated using SECM. The local electrocatalytic activity of **Tta-Dfp** towards the ODC was visualized *viz.* redox competition mode of SECM (Fig. 4a, RC-SECM). The four-electrode assembly consisted of a catalyst spot drop-coated over a glassy carbon (GC) plate (Fig. 4c) as WE2 with a Pt wire and Ag/AgCl/3 M KCl as the counter and reference electrode respectively. The local catalytic activity was probed in 0.4 HCl using the fourth electrode *i.e.*, the Pt-ultra-microelectrode (Ø 25 μm WE1) by polarizing both the tip and sample at the same potential of 0.2 V (*vs.* Ag/AgCl/3 M KCl) where the oxygen reduction takes place. Prior to the array scan measurements, tip positioning was ensured by measuring the approach curve (Fig. S20†). During the scanning in the *x*–*y* direction (Fig. 4b), when the tip passes from the unmodified GC surface to the active catalyst zone, tip (WE1) reduction current tends to decrease. This could be ascribed to the decreased O_2 availability at the catalyst spot which in turn signifies the superior catalytic activity of **Tta-Dfp**. The current response was collected at the Pt-tip and is represented as 2D and 3D images (Fig. 4), where the local ORR catalytic activity was illustrated with a color scheme changing from blue to green through yellow to red with decreasing tip current which can be ascribed to a higher ORR activity. The visualization of the local catalytic activity of **Tta-Dfp** and **Tab-Dfp** was performed by polarizing the sample at various potentials (−0.1, 0.0, 0.2 *vs.* RHE). 2D (Fig. 4d–f) and 3D SECM images in Fig. 4g–i and S21† exhibit notable differences in the ORR activity between **Tta-Dfp** and **Tab-Dfp**. As observed, a red color region (*i.e.*, more reduction in tip current) was clearly observed at a potential of 0.2 V, and upon moving towards more reduction potentials, the excellent catalytic activity of **Tta-Dfp** was observed even compared to **Tab-Dfp**. Furthermore, the line scans for all the scanned plots (Fig. S22†) clearly indicate the increasing competition of the catalysts towards the ORR at higher reduction potentials.

However, local electrocatalytic activity was also assessed for **Tab-Dfp** and higher tip current was observed as compared to **Tta-Dfp**.

Besides the activity, the catalysts were highly stable which was witnessed from the array scan measurement performed in the *x*–*y* direction. For the same, two distinct pulse potential profiles were applied to the Pt tip (WE1) as schematically shown

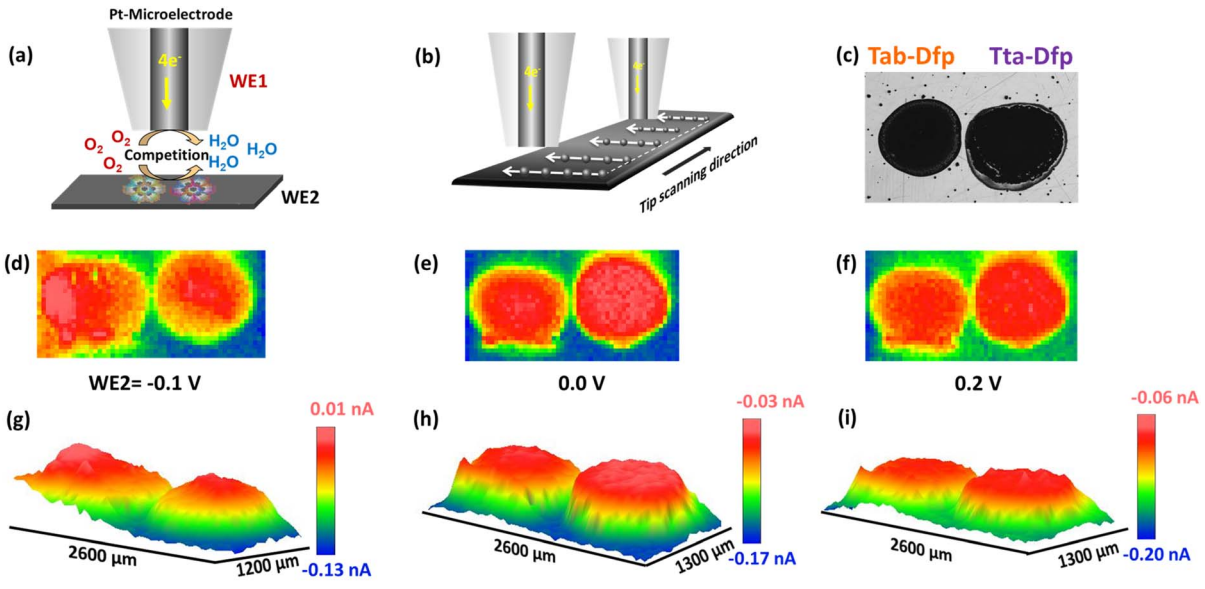

Fig. 4 (a) Schematic representation of RC-SECM mode (WE1: Pt microelectrode and WE2: catalyst coated GC plate), (b) SECM array scan, (c) microscopic images of **Tta-Dfp** and **Tab-Dfp** over the GC plate, 2D RC-SECM images of **Tta-Dfp** and **Tab-Dfp** spots measured in 400 mM HCl with different applied sample potentials: (d) −0.1 V, (e) 0.0 V, (f) 0.2 V and (g–i) their corresponding 3D images respectively. The tip (Pt-microelectrode) was polarized at 0.2 V.

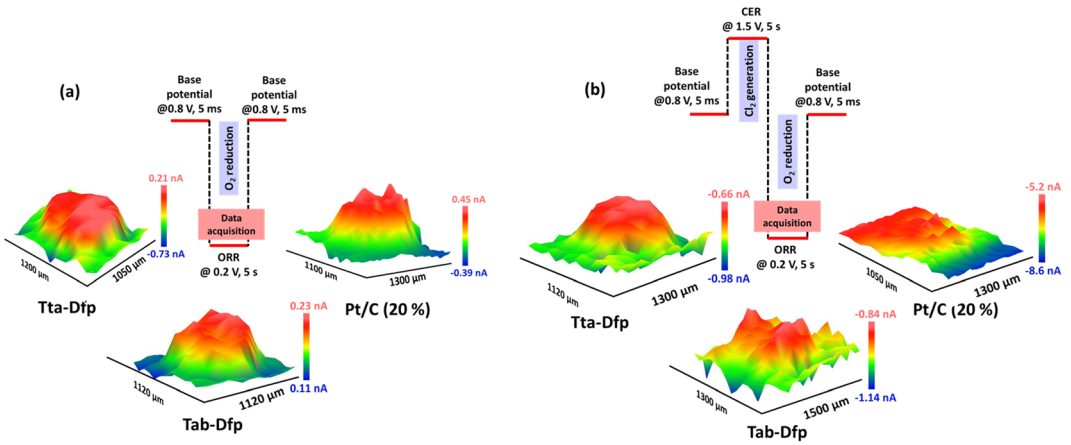

Fig. 5 Potential pulse profile for (a) only the ORR and (b) Cl_2 generation followed by the ORR at the Pt-tip and the corresponding 3D RC-SECM images of **Tta-Dfp**, **Tab-Dfp** and Pt/C (20%) measured in 400 mM HCl.

in Fig. 5a and b and the corresponding current response was recorded at the tip. In both the pulse profiles, the base potential (where WE1 is at rest) was chosen by recording the current at the tip with increasing potentials (Fig. S23a†). The obtained data in Fig. S23a† were further processed to obtain absolute current (absolute difference between the current measured before the first pulse and at the end of each sequential pulse) as a function of applied potential (Fig. S23b†). During the pulse profile as shown in Fig. 5a, the tip was subjected to the ORR (0.2 V) for 5 s after a base potential (0.8 V) of 5 ms while WE2 was constantly polarised at 0.2 V. As shown in Fig. 5a, **Tta-Dfp** showed higher activity as compared to **Tab-Dfp**. For comparison, the activity of the state-of-the-art catalyst of the ORR (Pt/C (20%)) was also probed using the same pulse profile. Towards the development of HCl electrolysers, a potential electrocatalyst is required with high stability; therefore accelerated degradation measurements have become mandatory. Therefore, to check the stability of both the catalysts along with Pt/C in chlorine and chloride ion rich environments, the pulse profile shown in Fig. 5b was applied on the Pt tip, wherein the ORR (0.2 V, 5 s) was preceded by the CER (1.5 V, 5 s) and base potential (0.8 V, 5 ms). As shown in Fig. 5b, the ORR activity of all the catalysts decreased, as compared to the first pulse profile, due to the replacement of localised O_2 with the Cl_2 generated

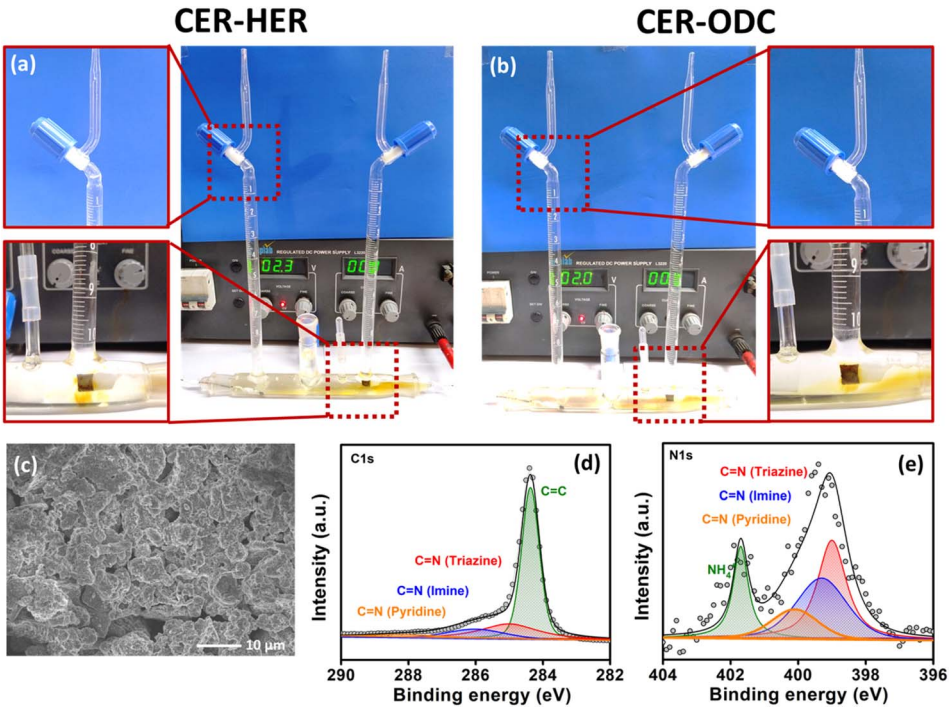

Fig. 6 Photographs displaying (a) HER coupled CER and (b) ODC coupled CER, (c) FE-SEM image and deconvoluted XPS spectra: (d) C 1s and (e) N 1s of **Tta-Dfp** after HCl electrolysis.

during the second pulse profile. However, current at the Pt/C spot degraded whereas **Tta-Dfp** and **Tab-Dfp** demonstrated a stable current response. Moreover, this was also visualised from the optical microscopic images for **Tta-Dfp**, **Tab-Dfp** and Pt/C spots before and after the SECM analysis (Fig. S24†). No degradation in **Tta-Dfp** and **Tab-Dfp** was observed whereas Pt/C degraded due to the dissolution of Pt from the catalyst into the solution,[21] demonstrating the superior activity of **Tta-Dfp** towards HCl electrolysis in Cl_2 rich electrolyte.

Full cell investigation. Encouraged by the excellent CER activity and the advanced ODC behaviour of **Tta-Dfp**, a two-electrode full cell was configured towards evaluating overall HCl electrolysis, in which **Tta-Dfp** worked as both the anode and cathode. The LSV in Fig. S25a† exhibited a cd of 6 mA cm^{-2} at a cell voltage of 2 V. Moreover, to assess the efficacy of **Tta-Dfp** in practical systems and under industrial conditions a CER coupled ODC system was assembled in a homemade designed cell equipped with burettes having a two-electrode setup in O_2 saturated 0.4 M HCl electrolyte. For comparison, a CER coupled HER system was constructed using a similar cell set up and Cl_2 production was visually analysed through a color change in the electrolyte upon addition of excess KI. As shown in Fig. 6a and b, the CER coupled HER required 2.3 V of cell potential to produce Cl_2 and H_2 at the anode and cathode, respectively; in contrast, the CER coupled ODC setup manifested the Cl_2 production at 2.0 V of DC power supply only. Moreover, no H_2 was observed on the cathodic side upon replacement by the ORR. Therefore, these outcomes illustrate that the CER-ODC system consumes lower energy to produce equivalent Cl_2, confirming that it has crucial benefits over the CER-HER system. Additionally, the stability of these cells (CER-HER and CER-ODC) was assessed by performing chronopotentiometry at 10 mA cm^{-2} for 12 h each and a constant potential indicated towards the stable catalyst response (Fig. S25b†). Moreover, it was observed that the CER-ODC cell could achieve 10 mA cm^{-2} at a lower cell potential of ~1 V whereas the CER-HER cell required a cell voltage of ~2 V. Furthermore, the catalyst was analysed using FE-SEM and XPS to investigate the physical changes after HCl electrolysis. As shown in Fig. 6c–e, the morphology and electronic structure of **Tta-Dfp** remained the same, pointing towards the remarkable robustness of the catalyst under harsh acidic conditions.

Conclusions

In summary, we have designed *in situ* proton filtering **Tta-Dfp** and **Tab-Dfp** catalysts for HCl electrocatalysis for the production of chlorine. The designed catalysts were explored as bifunctional electrocatalysts towards both the ODC and CER under HCl electrolysis conditions. *In situ* proton filtering **Tta-Dfp** exhibited higher activity both in terms of onset potential and current density as an ODC simultaneously demonstrating its superior activity towards the CER and achieved high faradaic efficiency, *i.e.* 92% for the CER. **Tta-Dfp** shows excellent stability even under multiple shut-down controls under harsh acidic conditions. Furthermore, the visualization of the local electrocatalytic activity of the designed catalyst was performed by RC-SECM using a Pt ultra-microelectrode. The activity was also further extended to state-of-the-art Pt/C (20%) by RC-SECM and our proposed catalyst was shown to have excellent stability in harsh acidic circumstances. Therefore, being metal free, the developed **Tta-Dfp** electrocatalyst may offer a cost-effective bifunctional catalyst alternative to expensive noble-metal based electrocatalysts for HCl electrolysis.

Conflicts of interest

There are no conflicts to declare.

Acknowledgements

S. K. thanks CSIR (09/1005(0029)/2020-EMR-1) for fellowship. K. G. thanks the Prime Minister Research Fellowship (PMRF) for a fellowship. D. S. and R. K. C. acknowledge Khalifa University, Abu Dhabi, for the generous support of this research. S. M. thanks CSIR (09/1005(0045)/2020-EMR-1) for fellowship. DS acknowledges the financial support from the Khalifa University Competitive Internal Research Award (CIRA-2022). DS acknowledges resource support under the Center for Catalysis and Separations (CeCaS, grant RCII-2018-024). T. C. thanks the Science and Engineering Research Board (SERB, SPG/2021/002415). Dr Sushil Kumar, KU, is acknowledged for PXRD refinement. FESEM and XPS, Central Research Facility (CRF), IIT Ropar is acknowledged for characterization.

References

1 Y. Zhao, S. Gu, K. Gong, J. Zheng, J. Wang and Y. Yan, *Angew. Chem., Int. Ed.*, 2017, **56**, 10735–10739.
2 M. Moser, C. Mondelli, A. P. Amrute, A. Tazawa, D. Teschner, M. E. Schuster, A. Klein-Hoffman, N. López, T. Schmidt and J. Pérez-Ramírez, *ACS Catal.*, 2013, **3**, 2813–2822.
3 R. Stringer and P. Johnston, 2001.
4 A. M. Nielsen, L. A. T. Garcia, K. J. S. Silva, L. P. Sabogal-Paz, M. M. Hincapié, L. J. Montoya, L. Galeano, A. Galdos-Balzategui, F. Reygadas, C. Herrera, S. Golden, J. A. Byrne and P. Fernández-Ibáñez, *Int. J. Hyg. Environ. Health*, 2022, **244**, 114004.
5 *Centers for Disease Control and Prevention*, 2020, **https://www.cdc.gov/healthywater/drinking/public/water_disinfection.html?CDC_AA_refVal=https%3A%2F%2Fwww.cdc.gov%2Fhealthywater%2Fdrinking%2Fpublic%2Fchlorine-disinfection.html#print**.
6 *The Association of Pool & Spa Professionals*, 2011, **https://www.phta.org/pub/?id=08fa1535-1866-daac-1599fb-f1535e1639fbe1531c1530**.
7 M. A. Adefisoye and A. O. Olaniran, *Antibiotics*, 2022, **11**, 564.
8 J. Rook, *Water Treat. Exam.*, 1972, **21**, 259.
9 J. M. Symons, T. A. Bellar, J. K. Carswell, J. DeMarco, K. L. Kropp, G. G. Robeck, D. R. Seeger, C. J. Slocum, B. L. Smith and A. A. Stevens, *J.–Am. Water Works Assoc.*, 1975, **67**, 634–647.
10 U. E. Protection, *National Primary Drinking Water Regulations: Stage 2 Disinfectants and Disinfection Byproducts Rule*,

Environmental Protection Agency, 2006, pp. 388–493, https://www.federalregister.gov/documents/2006/01/04/06-3/national-primary-drinking-water-regulations-stage-2-disinfectants-and-disinfection-byproducts-rule.
11 X.-F. Li and W. A. Mitch, *Environ. Sci. Technol.*, 2018, **52**, 1681–1689.
12 TI Partners, *GlobeNewsWire*, 2023.
13 J. Pérez-Ramírez, C. Mondelli, T. Schmidt, O. F. K. Schlüter, A. Wolf, L. Mleczko and T. Dreier, *Energy Environ. Sci.*, 2011, **4**, 4786–4799.
14 D. Teschner, R. Farra, L. Yao, R. Schlögl, H. Soerijanto, R. Schomäcker, T. Schmidt, L. Szentmiklósi, A. P. Amrute, C. Mondelli, J. Pérez-Ramírez, G. Novell-Leruth and N. López, *J. Catal.*, 2012, **285**, 273–284.
15 K. Seki, *Catal. Surv. Asia*, 2010, **14**, 168–175.
16 J. Crook and A. Mousavi, *Environ. Forensics*, 2016, **17**, 211–217.
17 S. Lakshmanan and T. Murugesan, *Clean Technol. Environ. Policy*, 2014, **16**, 225–234.
18 M. Mortensen, R. G. Minet, T. T. Tsotsis and S. Benson, *Chem. Eng. Sci.*, 1996, **51**, 2031–2039.
19 C. Mondelli, A. P. Amrute, M. Moser, T. Schmidt and J. Pérez-Ramírez, *Chimia*, 2012, **66**, 694.
20 I. Garcia-Herrero, M. Margallo, R. Onandía, R. Aldaco and A. Irabien, *Sci. Total Environ.*, 2017, **580**, 147–157.
21 A. Maljusch, T. C. Nagaiah, S. Schwamborn, M. Bron and W. Schuhmann, *Anal. Chem.*, 2010, **82**, 1890–1896.
22 J. M. Ziegelbauer, A. F. Gullá, C. O'Laoire, C. Urgeghe, R. J. Allen and S. Mukerjee, *Electrochim. Acta*, 2007, **52**, 6282–6294.
23 C. Jin, W. Xia, T. C. Nagaiah, J. Guo, X. Chen, N. Li, M. Bron, W. Schuhmann and M. Muhler, *J. Mater. Chem.*, 2010, **20**, 736–742.
24 T. Vidakovic-Koch, I. G. Martinez, R. Kuwertz, U. Kunz, T. Turek and K. Sundmacher, *Membranes*, 2012, **2**, 510–528.
25 J.-L. Gustin, *Chem. Health Saf.*, 2005, **12**, 5–16.
26 A. F. Gullá, L. Gancs, R. J. Allen and S. Mukerjee, *Appl. Catal., A*, 2007, **326**, 227–235.
27 I. Moussallem, J. Jörissen, U. Kunz, S. Pinnow and T. Turek, *J. Appl. Electrochem.*, 2008, **38**, 1177–1194.
28 S. Bechtel, A. R. Crothers, A. Z. Weber, U. Kunz, T. Turek, T. Vidaković-Koch and K. Sundmacher, *Electrochim. Acta*, 2021, **365**, 137282.
29 R. J. Allen, J. R. Giallombardo, D. Czerwiec, E. S. De Castro and K. Shaikh, *US Pat.*, US6855660B2, 2000.
30 J. Zhang, Y. Yuan, L. Gao, G. Zeng, M. Li and H. Huang, *Adv. Mater.*, 2021, **33**, 2006494.
31 M. Janssen, P. Weber and M. Oezaslan, *Curr. Opin. Electrochem.*, 2023, **40**, 101337.
32 T. Schmidt, U. Paulus, H. A. Gasteiger and R. Behm, *J. Electroanal. Chem.*, 2001, **508**, 41–47.
33 A. Maljusch, T. C. Nagaiah, S. Schwamborn, M. Bron and W. Schuhmann, *Anal. Chem.*, 2010, **82**, 1890–1896.
34 Z. Zhou, Y. Kong, H. Tan, Q. Huang, C. Wang, Z. Pei, H. Wang, Y. Liu, Y. Wang, S. Li, X. Liao, W. Yan and S. Zhao, *Adv. Mater.*, 2022, **34**, 2106541.
35 V. Singh and T. C. Nagaiah, *J. Mater. Chem. A*, 2019, **7**, 10019–10029.
36 V. Singh, S. D. Adhikary, A. Tiwari, D. Mandal and T. C. Nagaiah, *Chem. Mater.*, 2017, **29**, 4253–4264.
37 D. Gupta, A. Kafle, A. Chaturvedi and T. C. Nagaiah, *ChemElectroChem*, 2021, **8**, 2858–2866.
38 Y. Liu, C. Li, C. Tan, Z. Pei, T. Yang, S. Zhang, Q. Huang, Y. Wang, Z. Zhou, X. Liao, J. Dong, H. Tan, W. Yan, H. Yin, Z.-Q. Liu, J. Huang and S. Zhao, *Nat. Commun.*, 2023, **14**, 2475.
39 Y. Wang, Y. Liu, D. Wiley, S. Zhao and Z. Tang, *J. Mater. Chem. A*, 2021, **9**, 18974–18993.
40 O. M. Yaghi, M. J. Kalmutzki and C. S. Diercks, *Introduction to Reticular Chemistry: Metal-Organic Frameworks and Covalent Organic Frameworks*, John Wiley & Sons, 2019.
41 G. Das, F. Benyettou, S. K. Sharama, T. Prakasam, F. Gándara, V. A. de la Peña-O'Shea, N. i. Saleh, R. Pasricha, R. Jagannathan, M. A. Olson and A. Trabolsi, *Chem. Sci.*, 2018, **9**, 8382–8387.
42 L. Zhang, L. Yi, Z.-J. Sun and H. Deng, *Aggregate*, 2021, **2**, e24.
43 C. Krishnaraj, A. M. Kaczmarek, H. S. Jena, K. Leus, N. Chaoui, J. Schmidt, R. Van Deun and P. Van Der Voort, *ACS Appl. Mater. Interfaces*, 2019, **11**, 27343–27352.
44 C. Krishnaraj, H. S. Jena, K. S. Rawat, J. Schmidt, K. Leus, V. Van Speybroeck and P. Van Der Voort, *ACS Appl. Mater. Interfaces*, 2022, **14**, 50923–50931.
45 K. C. Ranjeesh, S. Kaur, A. K. Mohammed, S. Gaber, D. Gupta, K. Badawy, M. Aslam, N. Singh, T. Skorjanc, M. Finšgar, J. Raya, T. C. Nagaiah and D. Shetty, *Adv. Energy Mater.*, 2024, 2303068, DOI: 10.1002/aenm.202303068.
46 C. G. Piscopo, C. M. Granadeiro, S. S. Balula and D. Bošković, *ChemCatChem*, 2020, **12**, 4721–4731.
47 S. Liu, T. Qian, M. Wang, H. Ji, X. Shen, C. Wang and C. Yan, *Nat. Catal.*, 2021, **4**, 322–331.
48 W. Zhao, P. Yan, B. Li, M. Bahri, L. Liu, X. Zhou, R. Clowes, N. D. Browning, Y. Wu, J. W. Ward and A. I. Cooper, *J. Am. Chem. Soc.*, 2022, **144**, 9902–9909.
49 W. Ai, X. Du, Y. Yang, Z. Zheng, L. Zhai, B. Ma, S. Cui, P. Li, L. Mi and L. Qu, *J. Mater. Chem. A*, 2022, **10**, 18602–18608.
50 A. M. Kaczmarek, H. S. Jena, C. Krishnaraj, H. Rijckaert, S. K. P. Veerapandian, A. Meijerink and P. Van Der Voort, *Angew. Chem., Int. Ed.*, 2021, **60**, 3727–3736.
51 J. Liu, Y. Hu and J. Cao, *Catal. Commun.*, 2015, **66**, 91–94.
52 L. Hao, S. Zhang, R. Liu, J. Ning, G. Zhang and L. Zhi, *Adv. Mater.*, 2015, **27**, 3190–3195.
53 T. Sönmez, K. S. Belthle, A. Iemhoff, J. Uecker, J. Artz, T. Bisswanger, C. Stampfer, H. H. Hamzah, S. A. Nicolae, M.-M. Titirici and R. Palkovits, *Catal. Sci. Technol.*, 2021, **11**, 6191–6204.
54 J.-D. Yi, R. Xu, Q. Wu, T. Zhang, K.-T. Zang, J. Luo, Y.-L. Liang, Y.-B. Huang and R. Cao, *ACS Energy Lett.*, 2018, **3**, 883–889.